

The Supergalactic Plane revisited with the Optical Redshift Survey

O. Lahav^{1,2}, B.X. Santiago³, A.M. Webster¹, Michael A. Strauss^{4,8},
M. Davis⁵, A. Dressler⁶ & J.P. Huchra⁷

¹ *Institute of Astronomy, Madingley Road, Cambridge, CB3 0HA*

² *Racah Institute of Physics, The Hebrew University, Jerusalem 91904, Israel; email: lahav@astro.huji.ac.il*

³ *Instituto de Física, Universidade Federal do Rio Grande do Sul, 91501-970, Porto Alegre, RS, Brazil*

⁴ *Princeton University Observatory, Princeton, NJ 08544, USA*

⁵ *Physics and Astronomy Departments, University of California, Berkeley, CA 94720, USA*

⁶ *Observatories of the Carnegie Institution, 813 Santa Barbara St., Pasadena, CA 91101, USA*

⁷ *Center for Astrophysics, 60 Garden St., Cambridge, MA 02138, USA*

⁸ *Alfred P. Sloan Foundation Fellow, and Cottrell Fellow of Research Corporation*

9 August 2013

ABSTRACT

We re-examine the existence and extent of the planar structure in the local galaxy density field, the so-called Supergalactic Plane (SGP). This structure is studied here in three dimensions using both the new Optical Redshift Survey (ORS) and the *IRAS* 1.2 Jy redshift survey. The density contrast in a slab of thickness of $20 h^{-1}$ Mpc and diameter of $80 h^{-1}$ Mpc aligned with the standard de Vaucouleurs' Supergalactic coordinates, is $\delta_{sgp} \sim 0.5$ for both ORS and *IRAS*. The structure of the SGP is not well described by a homogeneous ellipsoid, although it does appear to be a flattened structure, which we quantify by calculating the moment of inertia tensor of the density field. The directions of the principal axes vary with radius, but the minor axis remains within $\theta_z \sim 30^\circ$ of the standard SGP Z -axis, out to a radius of $80 h^{-1}$ Mpc, for both ORS and *IRAS*. However, the structure changes shape with radius, varying between a flattened pancake and a dumbbell, the latter at a radius of $\sim 50 h^{-1}$ Mpc, where the Great Attractor and Perseus-Pisces superclusters dominate the distribution. This calls to question the connectivity of the 'plane' beyond $\sim 40 h^{-1}$ Mpc. The configuration found here can be viewed as part of a web of filaments and sheets, rather than as an isolated pancake-like structure. An optimal minimum variance reconstruction of the density field using Wiener filtering which corrects for both redshift distortion and shot noise, yields a similar misalignment angle and behaviour of axes. The background-independent statistic of axes proposed here can be best used for testing cosmological models by comparison with N -body simulations.

Key words: galaxies: large scale structure

1 INTRODUCTION

The major planar structure in the local universe, the Supergalactic Plane (SGP), was recognized by de Vaucouleurs (1953, 1956, 1958, 1975a,b) using the Shapley-Ames catalogue, following an earlier analysis of radial velocities of nearby galaxies which suggested a differential rotation of the 'metagalaxy' by Rubin (1951). This remarkable feature in the distribution of nebulae was in fact already noticed by William Herschel more than 200 years earlier (for historical reviews see Flin 1986, Rubin 1989).

When referring to the SGP in this paper we mean the planar structure in the galaxy distribution. This should be

distinguished from the formal definition of Supergalactic coordinates. de Vaucouleurs *et al.* (1976, 1991) defined a spherical coordinate system L, B in which the equator roughly lies along the SGP (as identified at the time), with the North Pole ($B = 90^\circ$) in the direction of Galactic coordinates ($l = 47.37^\circ; b = +6.32^\circ$). The position $L = 0^\circ, B = 0^\circ$ is at ($l = 137.37^\circ, b = 0^\circ$), which is one of the two regions where the SGP is crossed by the Galactic Plane. The Virgo cluster is at ($L = 104^\circ; B = -2^\circ$). Traditionally, the Virgo cluster was regarded as the centre of an overdense region called the 'Local Supercluster' (e.g. Davis & Huchra 1982, Hoffman & Salpeter 1982, Tully & Shaya 1984, Lilje, Yahil

& Jones 1986). However, some of the much larger superclusters that are seen in recent redshift surveys, such as the Great Attractor and Perseus-Pisces, are near the SGP, and are possibly connected with the Local Supercluster, in the sense of being simply connected by an isodensity contour above the mean density (cf., Strauss *et al.* 1992; Strauss & Willick 1995; Santiago *et al.* 1995).

Although the SGP is clearly visible in whole-sky galaxy catalogues (e.g. Lynden-Bell & Lahav 1988; Lynden-Bell *et al.* 1988; Raychaudhury 1989; see also the references above), the extent of planar structure in the galaxy distribution in 3 dimensions has seen little quantitative examination in recent years. Tully (1986, 1987) claimed that the flattened distribution of clusters extends across a diameter of $\sim 0.1c$ with axial ratios of 4:2:1. Shaver & Pierre (1989) found that radio galaxies are more strongly concentrated to the SGP than are optical galaxies, and that the SGP as represented by radio galaxies extends out to redshift $z \sim 0.02$. Stanev *et al.* (1995) claimed that energetic cosmic rays arrive preferentially from the direction of the SGP, where potential sources (e.g. radio galaxies) are concentrated, but this result was criticized by Waxman, Fisher & Piran (1997). Di Nella & Paturel (1995) revisited the SGP using a compilation of nearly 5700 galaxies larger than 1.6 arcmin, and found indeed that galaxies were concentrated close to the Supergalactic Plane. Loan (1997) and Baleisis *et al.* (1998) searched for the SGP in projection in the 87GB (north) and PMN (south) radio surveys, and found signatures at the 1 and 3 σ levels, respectively.

The existence of a pancake-like structure has important theoretical implications. Gravity amplifies deviations from sphericity, i.e. an initial oblate homogeneous ellipsoid evolves into a disk, and an initial prolate structure ends up as a spindle (Lin, Mestel & Shu 1965). White & Silk (1979) modeled the Local Supercluster as a homogeneous ellipsoid in expanding universe, and considered implications for cosmological models and initial conditions. Although such a simple model is insightful, the structure of the SGP is far more complicated than a homogeneous ellipsoid, as we show below. In a more realistic cosmological scenario, where the primordial density field is Gaussian, non-spherical shapes are more abundant than spherical ones (Doroshkevich 1970, Bardeen *et al.* 1986), and hence are expected to appear at the present epoch as even more non-spherical. In the context of the ‘top-down’ Hot Dark Matter scenario, Zel’dovich (1970) showed that pancake-like structures are the natural outcome of gravitational instability in the quasi-linear regime. Further studies have indicated that a web of filaments could also form in hierarchical Cold Dark Matter (bottom-up) scenarios (e.g. Bond, Kofman & Pogosyan 1996), but the shapes look quite different in different scenarios, as a result of both initial conditions and the cosmic time which allows the perturbations to grow. Hence, quantitative measures of the SGP and other observed filamentary structures and superclusters (Bahcall 1988) could be very important in distinguishing between models, e.g. by applying the shape statistic to both data and to N -body simulations.

Here we study the properties of the SGP using the Optical Redshift Survey (ORS, Santiago *et al.* 1995) which provides the most detailed and uniform optically-selected sample of the local galaxy density field to date. For comparison, we also use the full-sky redshift survey of galax-

ies selected from the database of the *Infrared Astronomical Satellite* (*IRAS*), complete to 1.2 Jy at $60\mu\text{m}$ (Fisher *et al.* 1995a). In this paper we consider the approach of ‘moment of inertia’ (MoI) to quantify a planar structure (cf. Babul & Starkman 1992; Luo & Vishniac 1995; Dave *et al.* 1997; Sathyaprakash *et al.* 1998).

The outline of the paper is as follows. Section 2 describes the ORS and *IRAS* samples, while in Section 3 we discuss the visual impression and preliminary analysis of the SGP. Section 4 describes the formalism of the MoI we also develop related statistics which are independent of the background determination. Section 5 gives the results of MoI when applied to the samples, and Section 6 presents Wiener reconstruction of the MoI for *IRAS*. Section 7 gives interpretation of the results using mock realizations, and conclusions and future work are discussed in Section 8.

2 THE ORS AND IRAS SAMPLES

The Optical Redshift Survey (ORS, Santiago *et al.* 1995) covers the sky at Galactic latitude $|b| > 20^\circ$. The survey was drawn from the UGC (Nilson 1973), ESO (Lauberts 1982), and ESGC (Corwin & Skiff 1995) galaxy catalogues, and it contains two subsets: one complete to a blue photographic magnitude of 14.5, and the other complete to a blue major diameter of 1.9 arcmin. The entire sample consists of 8457 galaxies, with redshifts available for 98% of them; ≈ 1300 new redshifts were measured to complete the survey. The high number density of galaxies in ORS makes it ideal for cosmographical studies of the local universe.

As ORS only covers $|b| > 20^\circ$, we filled in the Zone of Avoidance (ZOA) at $|b| < 20^\circ$ with galaxies from the *IRAS* 1.2 Jy survey (Fisher *et al.* 1995a). The Zone of Avoidance in *IRAS*, $|b| < 5^\circ$, was filled by interpolation based on the observed galaxy distribution below and above the ZOA (Yahil *et al.* 1991). While in principle it is possible to interpolate for the ORS ZOA, e.g. by hand or using a Wiener reconstruction (Lahav *et al.* 1994), we prefer to include real structure as probed by *IRAS* even at the price of mixing two different data sets. Hereafter when we refer to the ORS sample we mean that supplemented by the *IRAS* 1.2 Jy galaxies at $|b| < 20^\circ$.

Due to Galactic extinction and the diversity of catalogues used, the selection function of ORS depends on both distance and direction (Santiago *et al.* 1996). In order to account for these selection effects, a weight is usually associated with each galaxy. For a uniform survey like *IRAS* (see below) the selection function ϕ depends only on the distance to a galaxy, $|\mathbf{x}|$, and hence the weight is simply

$$w_{gal} = \frac{1}{\langle n \rangle \phi(|\mathbf{x}|)}, \quad (1)$$

where the mean number density of galaxies is estimated by

$$\langle n \rangle = \frac{1}{V} \sum_{gal} 1/\phi(|\mathbf{x}|) \quad (2)$$

(see Davis & Huchra 1982 for an alternative minimum variance estimator of the mean density).

For ORS, we follow Santiago *et al.* (1996) and Hermit

et al. (1996) and weight each galaxy by:

$$w_{gal} = \frac{1}{\langle n \rangle_{\mu} \phi(\mathbf{x})} \frac{\langle n \rangle_{\mu, iras}}{\langle n \rangle_{tot, iras}}, \quad (3)$$

where μ labels the catalogue from which the galaxy in question is drawn; each of the four catalogues making up the ORS has its own mean density $\langle n \rangle_{\mu}$. Here $\langle n \rangle_{\mu, iras}$ is the mean number density of *IRAS* galaxies in the volume corresponding to the μ -th catalogue in ORS. This brings each of the subsamples, with their separate selection criteria, to a uniform weighting (Santiago *et al.* 1996). With the weighting of equation (1) or (3), we can thus calculate the galaxy density fluctuation field $\delta(\mathbf{x}) \equiv (\rho(\mathbf{x}) - \langle \rho \rangle) / \langle \rho \rangle$ throughout the volume surveyed.

For comparison we also apply our analysis to the complete *IRAS* 1.2 Jy sample (Fisher *et al.* 1995a; Strauss *et al.* 1992), which includes 5313 galaxies over 87.6 % of the sky. The ZOA in *IRAS* was interpolated according to the Yahil *et al.* (1991) procedure mentioned above. Hereafter we refer to this sample as the *IRAS* sample. We note that the ORS and *IRAS* samples are not really independent; roughly 60% of the *IRAS* 1.2 Jy galaxies out to $80 h^{-1}$ Mpc are also catalogued in the ORS magnitude limited sample.

We work purely in Local Group redshift space, except in section 6 on Wiener reconstruction.

3 A BRIEF TOUR OF THE SGP

3.1 Visual impression

Historically, the SGP was identified in projected 2-D maps. We used the *IRAS* sample (which is homogeneous over the sky) to revisit the 2-D appearance of the SGP by fitting the data to a great circle. For a projected distribution of sources the great circle along which the density of galaxies is enhanced can be found by calculating the covariance matrix: $I_{ij} = \sum_{gal} \hat{x}_i \hat{x}_j$ where the Cartesian axes \hat{x}_i ($i = 1, 2, 3$) are defined for a unit sphere. The matrix I_{ij} can be diagonalised (cf. Section 4.2) and the smallest eigen-vector indicates the direction of the normal to the great circle. We considered the projected *IRAS* galaxy distribution out to $40 h^{-1}$ Mpc and $80 h^{-1}$ Mpc, and found that the great circle is aligned with the standard de Vaucouleurs' SGP to within 19° and 7° respectively. Can we see the translation of the great circle to a plane in 3-dimensions? Figure 1 shows the raw distributions, uncorrected for selection effects of ORS and *IRAS* galaxies in a sphere of radius of $40 h^{-1}$ Mpc projected on the standard (*SGX-SGZ*), (*SGX-SGY*) and (*SGY-SGZ*) planes. The SGP is particularly visible edge-on in the (*SGX-SGZ*) and (*SGY-SGZ*) projections. We note that the structures seen in ORS and *IRAS* are quite similar, but the ORS map is much denser, and clusters are more prominent. Maps of the smoothed density field, after applying the appropriate weights, are shown elsewhere for the *IRAS* survey (Saunders *et al.* 1991; Strauss *et al.* 1992; Fisher *et al.* 1995b; Strauss & Willick 1995; Webster, Lahav & Fisher 1997) and for ORS (Santiago *et al.* 1995, 1996; Baker *et al.* 1998). In Figures 2 and 3 we show histograms of the galaxy density field δ , corrected for selection effects, as a function of *SGZ*, averaged over *SGX* and *SGY*, within spheres of ever-larger radii, as indicated in each panel. The SGP is seen as an enhancement

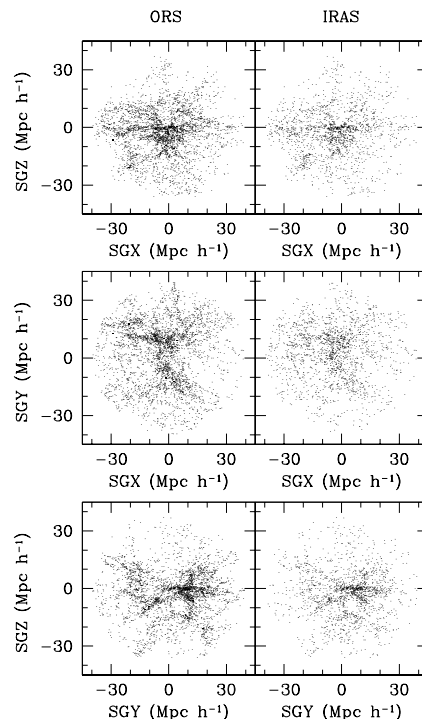


Figure 1. The distributions of ORS and *IRAS* galaxies in a sphere of radius of $40 h^{-1}$ Mpc, projected on the standard (*SGX-SGZ*), (*SGX-SGY*) and (*SGY-SGZ*) planes. The SGP is visible edge-on as the linear feature at *SGZ* = 0 in the (*SGX-SGZ*) and (*SGY-SGZ*) projections.

at *SGZ* = 0 in these plots to roughly $R_{max} = 60 h^{-1}$ Mpc, but is not apparent on larger scales.

3.2 The level of overdensity

Our visual impression is that there is indeed a flattened structure in the galaxy distribution, aligned along *SGZ* = 0, extending to appreciable redshifts. To quantify this we calculate the overdensity $\delta_{sgp} \equiv n_{sgp} / \langle n \rangle - 1$ as a function of R_{max} , where n_{sgp} is evaluated within a circular cylinder centered on the Local Group with radius R_{max} and height along *SGZ* of $20 h^{-1}$ Mpc, and the mean density $\langle n \rangle$ is calculated within a sphere of radius R_{max} (including the slab). This overdensity reaches a maximum at $R_{max} = 40 h^{-1}$ Mpc (for which the volume of the slab is $\sim (46 h^{-1} \text{ Mpc})^3$), $\delta_{sgp}(40) = 0.48 \pm 0.06$ and 0.46 ± 0.09 for ORS and *IRAS*, respectively. At $R_{max} = 60 h^{-1}$ Mpc, $\delta_{sgp}(60) = 0.36 \pm 0.06$ and 0.26 ± 0.08 for ORS and *IRAS*, respectively. For reference, the rms fluctuations in cubes of volume $(40 h^{-1} \text{ Mpc})^3$ are $\delta_{rms} \sim 0.37$ and ~ 0.30 for optical (Stromlo/APM) and *IRAS* (1.2 Jy) surveys, respectively (Efstathiou 1993). Hence the fluctuation in galaxy counts in a slab aligned with the standard de Vaucouleurs' SGP is no more than $\sim 1.5 \sigma$ perturbation on scale of $\sim 40 h^{-1}$ Mpc. This implies that the SGP is only a modest perturbation on these large scales. The overdensity as a function of the *Z* component of the standard SGP is depicted in Figures 2 and 3.

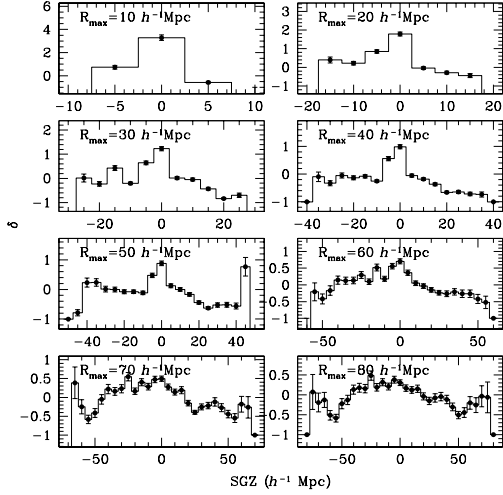


Figure 2. Histograms of the ORS density field (corrected for selection effects) as a function of SGZ , averaged over SGX and SGY , within spheres of radius as indicated in each panel. The error bars are Poissonian.

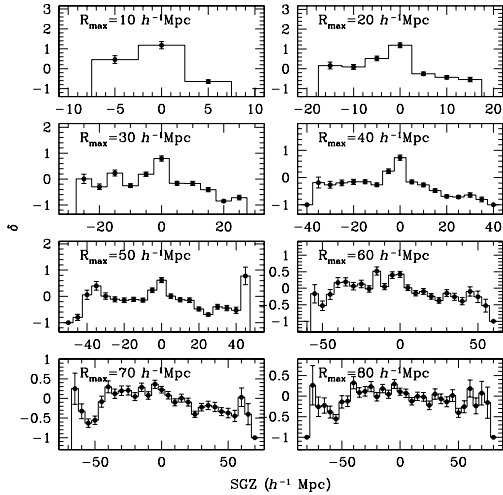


Figure 3. Histograms of the *IRAS* density field (corrected for selection effects) as a function of SGZ , averaged over SGX and SGY , within spheres of radius as indicated in each panel. The error bars are Poissonian.

3.3 The centre of the overdensity

In order to quantify the local overdensity, we need to calculate the centre of ‘mass’ of the density field, within a sphere of radius R_{max} centred on us, for both the ORS and *IRAS* samples (cf., Juskiewicz *et al.* 1990). The centre of mass is given by summing over the galaxies (assuming they all have equal mass):

$$\bar{x}_i = \frac{1}{V} \sum_{gal} w_{gal} x_i, \quad (4)$$

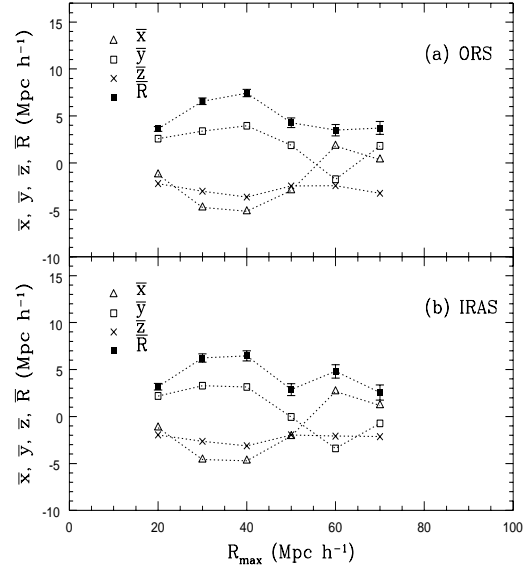


Figure 4. The variation of the mean position of the centre of mass of the galaxy distribution within a sphere of radius R_{max} centred on us, for both the ORS and *IRAS* samples. The curves show the Supergalactic x, y, z of the centre of mass, and its radial distance from the origin.

where $i = 1, 2, 3$, V is the total volume of the sphere of radius R_{max} and w_{gal} is the weight per galaxy described in §2. The shot noise error in each axis is

$$\sigma_{\bar{x}}^2 = \frac{1}{V^2} \sum_{gal} w_{gal}^2 x_i^2 = \frac{1}{3V^2} \sum_{gal} w_{gal}^2 r^2, \quad (5)$$

where the last equality is valid for an isotropic distribution. Figure 4 shows the coordinates of the centre of the galaxy distribution as a function of R_{max} . The centre moves away from the origin (the Local Group) by no more than $8 h^{-1}$ Mpc for ORS and $6 h^{-1}$ Mpc for *IRAS*. This is partially due to the ‘tug of war’ between the Great Attractor and Perseus-Pisces, which largely balance each other out. Indeed, the centre moves back towards the origin for $R_{max} > 40 h^{-1}$ Mpc.

4 PRINCIPAL COMPONENTS OF THE INERTIA TENSOR

Both visual impression of and a formal χ^2 fit suggest that the SGP cannot be fitted by a homogeneous ellipsoid model. We therefore seek a more objective measure of deviation from sphericity, via the Moment of Inertia tensor (MoI).

4.1 Estimation of the Moment of Inertia

We wish to detect a high density planar structure (e.g. a slab or an ellipsoid) embedded in a uniform sphere of radius R_{max} . One approach (cf. Babul & Starkman 1992, Luo & Vishniac 1995, Dave *et al.* 1997) is to construct the MoI for

the *fluctuation* in the density field:

$$\tilde{C}_{ij} = C_{ij} - \bar{C}_{ij} = \frac{1}{\langle n \rangle V} \int [n(\mathbf{x}) - n_{bg}] (x_i - \bar{x}_i) (x_j - \bar{x}_j) dV, \quad (6)$$

where $n(\mathbf{x})$ is the galaxy number density at position \mathbf{x} , $\langle n \rangle$ is the mean number density and x_i, x_j ($i, j = 1, 2, 3$) are Cartesian components of \mathbf{x} . Note that we allow the centre $\bar{\mathbf{x}}$ to move (see Figure 4), although below, we will end up keeping it fixed. The integration is over the volume of the sphere. We define the fluctuations in the density field relative to the *background* density n_{bg} in the absence of the slab (which differs from the mean density $\langle n \rangle$ including the slab).

For a uniform distribution with density $\langle n \rangle$ the covariance matrix is analytic and isotropic:

$$\begin{aligned} \bar{C}_{ij} &= \frac{f_{bg}}{V} \int x_i x_j dV = \frac{1}{3} \delta_{ij}^K \frac{f_{bg}}{V} \int_0^{R_{max}} r^2 (4\pi r^2 dr) = \\ &= \delta_{ij}^K f_{bg} \frac{R_{max}^2}{5}, \end{aligned} \quad (7)$$

where

$$f_{bg} \equiv \frac{n_{bg}}{\langle n \rangle}, \quad (8)$$

$\bar{\mathbf{x}}$ is of course zero, and δ_{ij}^K is the Kronecker delta function.

For a discrete density field, such as provided by ORS or IRAS, we can calculate the covariance elements by summing over the galaxies:

$$\tilde{C}_{ij} = C_{ij} - \bar{C}_{ij} = \frac{1}{V} \sum_{gal} w_{gal} x_i x_j - \delta_{ij}^K f_{bg} \frac{R_{max}^2}{5}, \quad (9)$$

where we have set $\bar{\mathbf{x}} = 0$, given the fact that the centre of mass stays so close to the origin (Figure 4). An analytic estimator for Poisson shot-noise per diagonal component of the covariance matrix (assuming no errors in f_{bg}) is:

$$\sigma_c^2 = \frac{1}{(3V)^2} \sum_{gal} w_{gal}^2 r^4. \quad (10)$$

Eq. (9) requires knowledge of f_{bg} in order to correct for the background density. However, as the boundaries of the SGP are hard to define *a priori* and the background will not be uniform, it is difficult to estimate a meaningful f_{bg} . In §4.3 we suggest a statistic which is independent of this parameter.

4.2 Principal axes

The next step in our analysis is to diagonalize the MoI and find the eigenvalues λ_α and associated eigenvectors \mathbf{u}_α ($\alpha = 1, 2, 3$):

$$\tilde{C} \mathbf{u}_\alpha = \lambda_\alpha \mathbf{u}_\alpha. \quad (11)$$

The standard deviation ('1- σ ') along each of the three axes is given by $\sqrt{\lambda_\alpha}$, which we label hereafter as a, b, c . Note that since the background contribution (the last term in eq. 9) is isotropic, it only affects the eigenvalues, but not the directions of the eigenvectors. This procedure is essentially the Principal Component Analysis (PCA) - a well known statistical tool for reducing the dimensionality of parameter

space (e.g. Murtagh & Heck 1987 and references therein). By identifying the *linear* combination of input parameters with maximum variance, PCA determines the Principal Components that can be most effectively used to characterize the input data. In our case, in searching for a plane, we wish to see if the PCA finds one axis to be much shorter than the other two axes.

4.3 Background-independent statistic of axes

Our aim is to quantify deviations from spherical structure. The difficulty in doing so is due to two problems: (i) the background density as modeled above with f_{bg} is ill-determined, and (ii) the shot noise due to the finite number of galaxies can be quite large.

We will discuss the shot noise problem in §6 below. To overcome the problem of the unknown background, we can construct the following quantities which are independent of f_{bg} :

$$p^2 = |a^2 - b^2|, \quad (12)$$

$$q^2 = |a^2 - c^2|. \quad (13)$$

and

$$s^2 = |b^2 - c^2|. \quad (14)$$

For a perfect sphere, $p = q = s = 0$. For a homogeneous oblate ellipsoid with semi-major axes $A = B > C$, one expects $p = 0$ for all R_{max} , but for q and s to increase out to $R_{max} \approx A$ and then to decline. Note that the (p, q, s) here are in the diagonalized PCA frame, where the axes are ordered by size ($a \geq b \geq c$). Alternatively, we can calculate (p, q, s) along fixed (x, y, z) axes (e.g. in de Vaucouleurs' system) by replacing a^2, b^2, c^2 in eqs. (12-14) by the non-ordered variances in that fixed coordinate system (i.e. the diagonal elements in the MoI matrix in that (x, y, z) coordinate system).

In the limit that the errors are isotropic the Poisson error bars are:

$$\Delta p = \sigma_c^2 / p, \quad (15)$$

and similarly for q and s . We will determine the characteristic shape of the galaxy density field, from the observed p, q and s and their error bars as a function of R_{max} . We note that other transformations of (a, b, c) are possible, such as the $(S1, S2, S3)$ statistic proposed by Babul & Starkman (1992).

4.4 Mock realizations

To get an insight into our (p, q, s) statistic we applied it to mock realizations of ellipsoids placed in a uniform background. The IRAS selection function was applied to the mock samples, and the results were averaged over 100 realizations. Figure 5 shows the quantities p, q , and s derived at fixed axes for mock ellipsoids (oblate, prolate and triaxial) with dimensions indicated in the panels and overdensity of $\delta = 0.4$. When the axes were allowed to be chosen by PCA, the axes agreed with the correct orientation of the ellipsoids

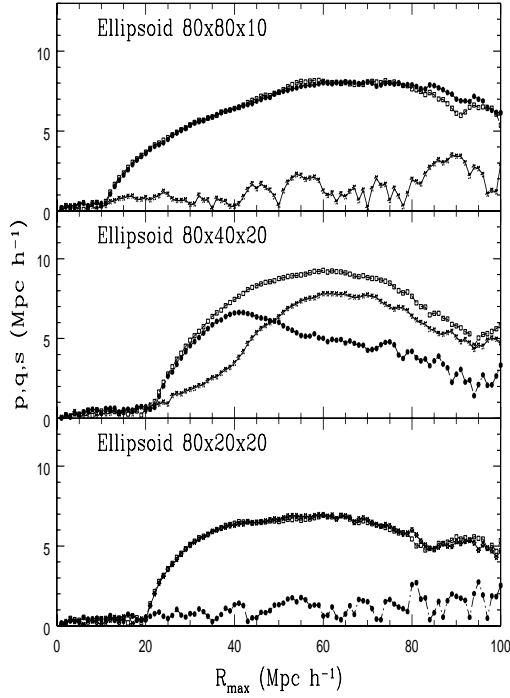


Figure 5. The quantities p (crosses), q (open squares) and s (filled circles) given by eqs. (12-14) vs. R_{max} for mock ellipsoids (oblate, prolate and triaxial) with dimensions (in h^{-1} Mpc) indicated in the panels, all ellipsoids with density contrast of $\delta = 0.4$. The mock samples have an *IRAS* selection function, and the results are averaged over 100 realizations at fixed axes.

to within 7° (rms over 100 realizations). For a single realization the curves are much more noisy. Moreover, if PCA defines the axes, it attempts to maximize the differences between the axes, and the results for p, q , and s are biased by noise. For example, in the case of a perfectly oblate structure in the presence of noise, the quantity s increases with radius R_{max} , where it is identically zero in the noise-free case. Fortunately, we will see in the following section that the behaviour of (p, q, s) for the real data is quite robust. We will continue these experiments with the mock realizations in §7, where we consider more complex geometries.

5 APPLICATION OF MOI TO ORS AND IRAS

We now apply the MoI approach to the ORS and *IRAS* samples. We begin by considering p, q , and s along *fixed* axes. We will find below that the PCA direction at small R_{max} is indeed very close to that of de Vaucouleurs' system, so we simply choose the standard de Vaucouleurs' SGP axes. Figure 6 shows p, q and s (derived here from the variances along the standard SGP axes without ordering them, as explained in section 4.3) as a function of R_{max} . The most notable feature is the dip in s at about $R_{max} = 50 h^{-1}$ Mpc in both samples. This is due to the dumbbell-like configuration of Perseus-Pisces and the Great Attractor on opposite sides of the sky, as we'll see in §7. But at $R_{max} = 80 h^{-1}$ Mpc, the structure is pancake-like: p tends to small values (in

particular in ORS), more in line with the visual impression of a pancake-like structure in Figure 1. However, the dramatic changes with R_{max} (in particular at $50 h^{-1}$ Mpc) call to question the notion of a single coherent feature within the boundaries of our samples (see §7). Based on Figure 6, one may argue that the 'plane' terminates at $\sim 40 h^{-1}$ Mpc.

We now turn to the PCA approach of diagonalizing the MoI derived at each radius R_{max} . In this case the axes change direction, and might even 'swap'. 'Swapping' means that an axis which is the largest at a given R_{max} may become say the second or third largest in a different R_{max} . Hence we may see a discontinuity in the variation of the 'largest' axis with R_{max} .

The variation at large R_{max} is more difficult to interpret, but we see that $q > p > s$, implying a triaxial shape, and p and q increase with R_{max} . In contrast, the toy models (Figure 5) show that two of $[p, q, s]$ drop with R_{max} beyond the radius which encloses the ellipsoid ($80 h^{-1}$ Mpc in the toy models). But in making this comparison with Figure 5 we should keep in mind that at large R_{max} the increase of the observed quantities p, q or s might be due to shot-noise. It is also interesting to note the similarity between ORS and *IRAS*, indicating that on the very large scales the density fields in the two samples are quite similar.

Table 1 lists a, b, c , their Poisson errors, and the direction of the PCA Z component for ORS (for direct summation) and *IRAS* (for both direct summation and Wiener reconstruction described in the next Section). Table 1 also lists the values in *differential* shells, showing trends similar to those seen in the cumulative plots.

Fig 9 shows the variation of direction of the PCA Z component with R_{max} . We see that although the angle $\theta_z \equiv 90^\circ - B_z$ between the PCA minor axis and de Vaucouleurs' pole is usually less than 30° , there is a significant variation on the sky (relative to the errors of $\sim 10^\circ$ due to shot noise). Particularly noticeable is the big jump at $R_{max} = 50 h^{-1}$ Mpc, in accord with the behaviour in Figures 6, 7 and 8. This is again due to the dumbbell configuration of the Great Attractor and the Perseus-Pisces superclusters, as we shall see in §7. Table 1 also gives B_z , the complement of the misalignment angle θ_z , for 3 shells, each $20 h^{-1}$ Mpc wide. We see that indeed typically $\theta_z \sim 30^\circ$, even at the $(60-80) h^{-1}$ Mpc shell, which is beyond the Great Attractor and Perseus-Pisces. The probability that two random vectors are separated by an angle less than $\theta_z \sim 30^\circ$ by chance is $P(< \theta_z) = [1 - \cos(\theta_z)]$, i.e. $\sim 13\%$.

6 WIENER RECONSTRUCTION

In addition to the problem of shot-noise, the density field measured from redshift surveys also suffers from redshift distortions due to peculiar velocities (see Hamilton 1998 for a review). One approach which deals with both problems is Wiener filtering (e.g. Lahav *et al.* 1994, Fisher *et al.* 1995b). In particular, Fisher *et al.* (1995b) expanded the density field $\delta(\mathbf{r})$ in terms of spherical harmonics and Bessel functions. By assuming a prior model for the power spectrum, the coefficients of the expansion can be corrected for the redshift distortion and for the shot-noise. This reconstruction is optimal in the minimum variance sense. In this approach, the smoothed density field approaches the mean

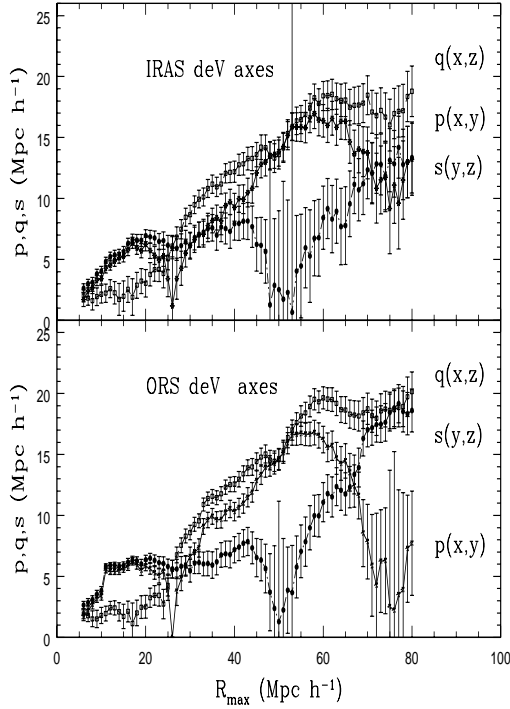


Figure 6. The quantities (p, q, s) derived from the variances along the de Vaucouleurs' axes vs. R_{max} (cumulative) for the ORS and *IRAS* samples. The error bars are Poisson.

density at large distances. This does not mean necessarily that the SGP itself disappears at large distances; it merely reflects our ignorance of the density field where the data are poor.

This Wiener approach applied to the density field δ also gives the optimal reconstruction for any property which is linear in δ . In particular, if we seek the optimal reconstruction of the moment of inertia (eq. 7) it can be re-written (for $\bar{x} = 0$) as

$$\tilde{C}_{ij} = \left(\frac{3}{4\pi R_{max}^3} \right) I_{ij} + [1 - f_{bg}] \frac{R^2}{5} \delta_{ij}^K \quad , \quad (16)$$

where

$$I_{ij} = \int_R \delta(\mathbf{r}) x_i x_j dV \quad . \quad (17)$$

Webster, Lahav & Fisher (1997) give analytic expressions for I_{ij} in terms of the reconstructed coefficients δ_{lmn}^R , and show that only harmonic modes $l = 0$ and $l = 2$ contribute.

We apply this technique below to the reconstructed, real-space density field of *IRAS* galaxies, assuming as priors $\beta \equiv \Omega^{0.6}/b = 0.7$, normalization $\sigma_8 = 0.7$ and a CDM power spectrum with shape parameter $\Gamma = 0.2$.

Figure 10 shows the p, q and s for *IRAS* before and after Wiener filtering in spherical harmonic presentation. Figure 11 shows the variation of the minor PCA axis with R_{max} . There is good agreement with the results of direct summation shown in Figure 9, indicating that shot noise and redshift distortion do not introduce big systematic effects in our statistics. Unfortunately, the Wiener procedure cannot

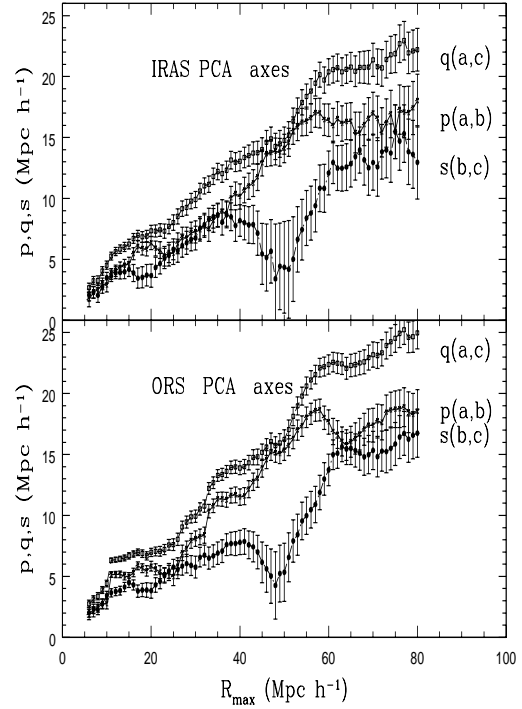


Figure 7. The quantities (p, q, s) derived from PCA dimensions (a, b, c) (eqs. 12-14) vs. R_{max} (cumulative) for the ORS and *IRAS* samples. The error bars are Poisson.

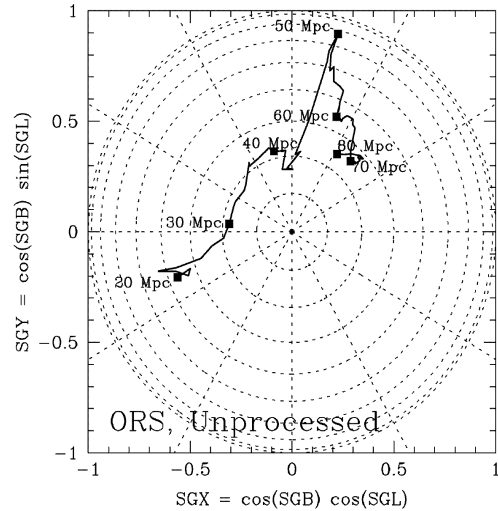


Figure 8. ORS : The direction of the Z axis from the PCA analysis (using direct summation over the galaxies) relative to the de Vaucouleurs' pole. Values of R_{max} are indicated.

easily be applied to the ORS sample, as it only covers $|b| > 20^\circ$.

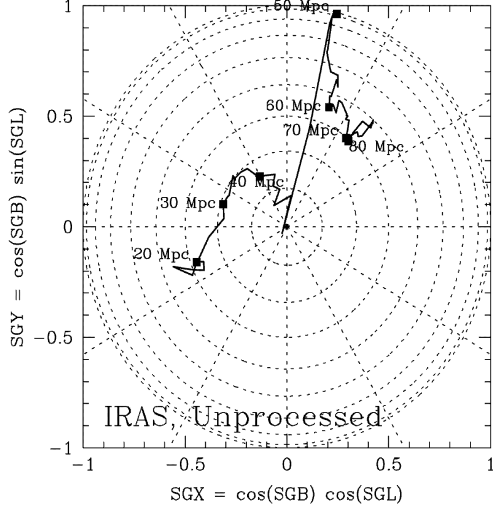


Figure 9. *IRAS*: The direction of the Z axis from the PCA analysis (using direct summation over the galaxies) relative to the de Vaucouleurs' pole. Values of R_{max} are indicated.

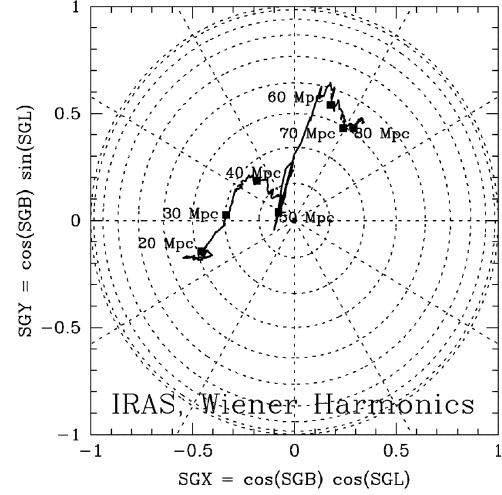


Figure 11. Wiener filtering of *IRAS*: The direction of the Z axis (as found by PCA) relative to the de Vaucouleurs' pole. Values of R_{max} are indicated.

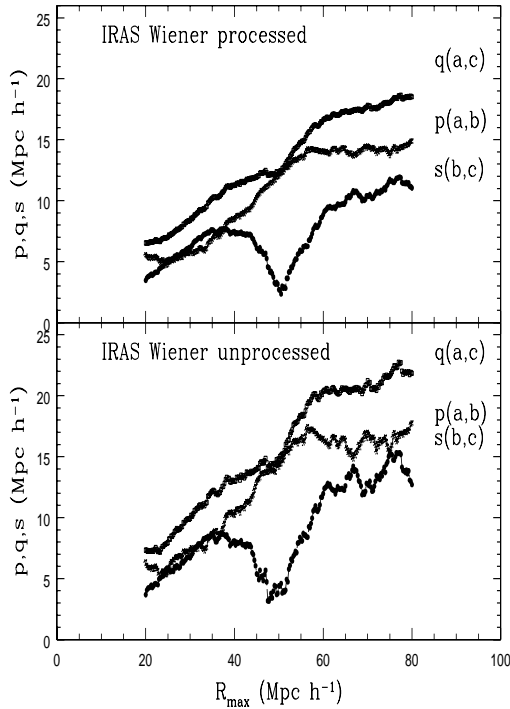


Figure 10. The quantities p, q, s vs. R_{max} (cumulative) in PCA axes using spherical harmonic reconstruction of *IRAS* and analytic MoI. Top: corrected for redshift distortion and noise by Wiener filtering, with parameters $\beta = 0.7, \Gamma = 0.2, \sigma_s = 0.7$ (reconstruction out to $200 h^{-1}$ Mpc). Bottom: using raw harmonics.

7 INTERPRETATION OF THE MOI RESULTS

The behaviour of the MoI axes (Figures 6-10) for both ORS and *IRAS* indicate that the SGP is a structure far more complicated than a homogeneous ellipsoid or a slab. In the local universe there is ‘contamination’ due to clusters and voids below and above the SGP. To get further insight to the structure that generates the observed MoI, we generated mock realizations of the *IRAS* sample with more complicated geometries than the simple ellipsoids used in §4.4, trying to mimic the significant overdensities seen in the real universe. In particular, we put in: (i) an ellipsoid with dimensions of $70 \times 70 \times 10 (h^{-1} \text{ Mpc})^3$ and overdensity $\delta = 1$ aligned with the Supergalactic plane, (ii) a sphere of radius $7.5 h^{-1}$ Mpc and overdensity $\delta = 2.5$, representing a Virgo-like cluster at $(SGX, SGY, SGZ) = (5, 10, -2) h^{-1}$ Mpc, (iii) a sphere of radius $11 h^{-1}$ Mpc and overdensity $\delta = 3$, representing a Perseus-Pisces-like supercluster at $(SGX, SGY, SGZ) = (49, -23, 0) h^{-1}$ Mpc, and (iv) a sphere of radius $10 h^{-1}$ Mpc and overdensity $\delta = 3$, representing a Great Attractor-like structure at $(SGX, SGY, SGZ) = (-32, 0, 0) h^{-1}$ Mpc.

Figure 12 shows (p, q, s) averaged over 100 realizations in fixed and PCA coordinates. It is interesting to contrast this Figure with Figures 6, 7 and 10. For example we see that the dips in s at $\sim 25 h^{-1}$ Mpc $50 h^{-1}$ Mpc in the real data (Figure 6) are reproduced here (albeit with not quite the same amplitudes), especially with fixed axes. This toy example illustrates that the observed behaviour of p, q , and s can be accounted for by adding few major superclusters to a pancake-like structure. We note that the toy model in Figure 12 does not reproduce the observed growth of p, q and s on large scales, which might be due to shot noise.

We note that recent simulations for a variety of models (e.g., Bond *et al.* 1996, Jenkins *et al.* 1998) show a web of filaments and sheets, with ‘knots’ at their intersection, or alternatively, ‘arms stretching from clusters’. It may well be that Perseus-Pisces and the Great Attractor represent such knots. Hence the MoI ‘shape-finder’ statistic, when ap-

Table 1. SGP parameters from PCA analysis

R_{min}	R_{max}	a	b	c	$\Delta(a^2)$	L_z	B_z
ORS							
0	20	9.9	8.1	7.1	2.4	160	53
0	30	14.8	12.4	11.0	5.1	173	72
0	40	19.9	16.2	14.3	7.7	104	68
0	50	25.8	20.7	20.0	12.7	76	23
0	60	31.8	26.5	22.7	17.8	67	56
0	70	35.6	31.1	27.0	24.1	48	65
0	80	39.8	35.2	31.0	33.0	58	65
20	40	21.7	17.7	15.4	9.5	101	66
40	60	35.1	29.2	24.8	23.7	65	55
60	80	45.8	40.3	36.2	57.4	52	68
IRAS							
0	20	10.3	8.1	7.2	3.4	160	62
0	30	14.9	13.0	11.1	6.6	162	71
0	40	19.6	16.8	14.7	10.6	120	75
0	50	25.5	21.3	20.8	16.4	76	-6
0	60	31.2	26.5	23.6	21.9	69	55
0	70	35.1	30.7	27.9	29.3	54	60
0	80	39.6	35.3	32.8	39.0	52	61
20	40	21.3	18.0	15.8	12.8	113	72
40	60	34.2	29.0	25.8	28.8	67	53
60	80	44.9	40.5	38.3	65.9	44	60
IRAS Wiener							
0	20	10.1	8.5	7.8	-	197	61
0	30	14.6	13.4	11.9	-	176	70
0	40	19.5	17.6	15.9	-	135	75
0	50	24.5	21.4	21.2	-	154	85
0	60	29.7	26.2	24.6	-	72	55
0	70	34.0	30.8	29.0	-	61	60
0	80	38.3	35.3	33.5	-	56	59

Comments on Table 1: R_{min} , R_{max} , a , b and c are in h^{-1} Mpc. The values of a , b and c are for $f_{bg} = 0$. The Poisson error per axis $\Delta(a^2)$ is derived using eqs. (15-17). No errors are given in the Wiener case, as this is a smoothed field (although one can calculate the scatter around the mean).

L_z and B_z (both in degrees) give the direction in standard de Vaucouleurs' coordinates of the Z component as found by PCA. The angle between this direction and de Vaucouleurs' SGP pole is simply $\theta_z = 90^\circ - B_z$.

plied to many points in space, could be an efficient way of detecting such patterns and discriminating between models.

8 CONCLUSIONS

We have presented a Moment of Inertia approach to study the existence and extent of the planar structure in the local galaxy density field, the Supergalactic Plane (SGP).

Our main conclusions from the present analysis are:

(i) The SGP is not well-modeled as a homogeneous ellipsoid.

(ii) The Moments of Inertia analysis of the galaxy density field shows that the normal to the plane is within $\theta_z \sim 30^\circ$ of the standard SGP Z -axis, out to a radius of $80 h^{-1}$ Mpc, for both ORS and IRAS. However, the normal changes direction with R_{max} , in particular at $\sim 50 h^{-1}$ Mpc,

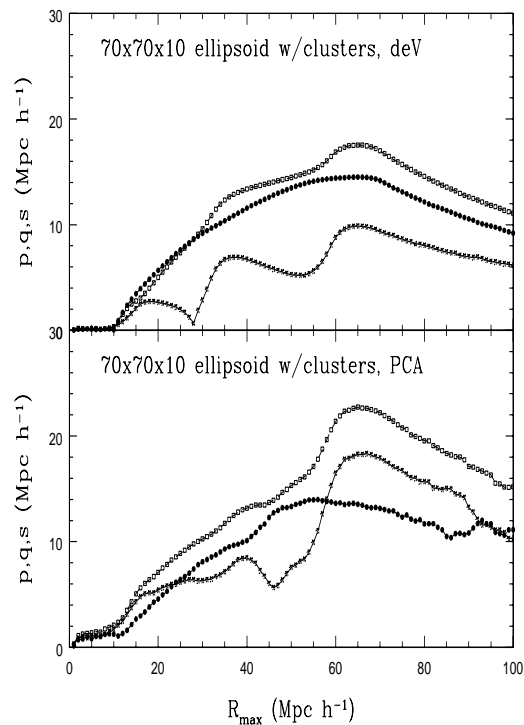


Figure 12. The quantities p , q , s vs. R_{max} (cumulative) in fixed and PCA axes for a mock realizations of an oblate ellipsoid plus three clusters, as described in the text. The upper panel uses fixed supergalactic coordinates, while the lower panel uses the axes found by the PCA analysis. Results were averaged over 100 realizations.

due to the presence of Perseus-Pisces and the Great Attractor. The shape too varies with R_{max} , and in fact at $50 h^{-1}$ Mpc the SGP looks more like a dumbbell than a pancake. Based on Figures 6, 7 and 10 one may argue that the 'plane' terminates at $\sim 40 h^{-1}$ Mpc. However, we note that the axes the shell $(60 - 80) h^{-1}$ Mpc are aligned with the standard SGP to within 30° .

(iii) The density contrast in the slab with $R_{max} = 40 h^{-1}$ Mpc and thickness of $20 h^{-1}$ Mpc centered on the Local Group and aligned along the Supergalactic axes is $\delta_{sgp} \sim 0.5$ for both ORS and IRAS.

(iv) The SGP axes and density contrast are similar for both ORS and IRAS.

(v) An optimal minimum variance reconstruction (Wiener filtering in spherical harmonics representation), which corrects IRAS for both redshift distortion and shot noise, yields similar misalignment of angle and axes.

(vi) It may well be that Perseus-Pisces and the Great Attractor represent 'knots' in a web of filaments and sheets, as seen in recent N -body simulations. This complicated structure calls to question the notion of a single coherent feature on Gpc scales (as claimed e.g. by Tully 1987, 1987), and the possible connectivity between the Great Attractor and the Shapley Supercluster at $\sim 140 h^{-1}$ Mpc (e.g. Scaramella *et al.* 1992).

Regarding the wider cosmological implications, the present analysis is as an example of applying the MoI at only

one point, centred at us. It is of interest to compare the SGP to other structures, e.g. the Great Walls seen in the CfA and SSRS surveys. One can calculate moments of inertia at many points in space and contrast the statistical behaviour of the axes with N -body simulations. Results from volume limited subsets of N -body simulations show indeed that the MoI statistic quantifies e.g. differences in filamentary structure between Cold and Hot dark matter models (e.g. Dave *et al.* 1997, Webster 1998). Unfortunately, the flux limited ORS and *IRAS* catalogues are too shallow to apply the statistic in other points in space. Volume limited subsets from new large redshift surveys (e.g. 2dF and SDSS) would be suitable for such shape-finding algorithms.

It also is possible to improve the above analysis by calculating the moment of inertia for a pre-selected region above a certain density-threshold. It would also be interesting to repeat the analysis for different morphological types and weighting schemes; for example, by calculating luminosity-weighted, rather than number weighted galaxy counts. On the statistical side, other more general shape-finders can be applied, e.g. by utilizing the Minkowski functions (e.g. Mecke, Buchert & Wagner 1994; Sahni, Sathyaprakash & Shandarin 1998).

Acknowledgments: We thank J. Bagla, A. Dekel, K. Fisher, D. Lynden-Bell, P. Monaco and S. Shandarin for helpful discussions and comments. MD acknowledges support from NSF grant AST95-28340. JPH was supported by the Smithsonian Institution and NASA NAGW-201. OL thanks the Weizmann Institute (Israel), the Anglo-Australian Observatory and ATNF/CSIRO (Australia) for their hospitality. MAS acknowledges support from the Alfred P. Sloan Foundation, Research Corporation, and NSF grant AST96-16901. AMW acknowledges the receipt of a PPARC studentship.

REFERENCES

- Babul, A. & Starkman, G.D. 1992, *ApJ*, 401, 28
Bahcall, N. 1988, *ARAA*, 26, 631
Baker, J.E., Davis, M., Strauss, M.A., Lahav, O. & Santiago, B.X., 1998, *ApJ*, in press (astro-ph/9802173)
Baleisis, A., Lahav, O., Loan, A.J., & Wall, J.V. 1998, *MNRAS*, 297, 545
Bardeen J.M., Bond J.R., Kaiser N., & Szalay A. 1986, *ApJ*, 304, 15
Bond, R. Kofman, L. & Pogosyan, D. 1996, *Nature*, 380, 606
Corwin, H.G. & Skiff, B.A. 1995, *Extension to the Southern Galaxies Catalogue*, in preparation
Dave, R., Hellinger, D., Primack, J., Nolthenius, R., & Klypin, A., 1997, *MNRAS*, 284, 607
Davis, M. & Huchra, J.P. 1982, *ApJ*, 254, 437
de Vaucouleurs, G. 1953, *AJ*, 58, 30
de Vaucouleurs, G. 1956, *Vistas in Astronomy*, 2, 1584
de Vaucouleurs, G. 1958, *ApJ*, 63, 223
de Vaucouleurs, G. 1975a, *ApJ*, 202, 610
de Vaucouleurs, G. 1975b, *ApJ*, 202, 616
de Vaucouleurs, G., de Vaucouleurs, A., Corwin, H.G., Jr. 1976, *The Second Catalogue of Bright Galaxies*, University of Texas Press, Austin
de Vaucouleurs, G., *et al.* 1991 *The Third Catalogue of Bright Galaxies (RC3)*, University of Texas Press, Austin
Di Nella, H., & Paturel, G. 1995, *Publ. Astron. Soc. Aust.*, 12, 26
Doroshkevich, A.G. 1970, *Astrophysica*, 6, 320
Efsthathiou, G. 1995, *Les Houches Lectures*, ed. R. Schaefer (Netherlands: Elsevier Science Publishers), 133
Fisher K.B., Huchra J.P., Davis M., Yahil A., & Schlegel D. 1995a, *ApJS*, 100, 69
Fisher K.B., Lahav O., Hoffman Y., Zaroubi S., & Lynden-Bell D., 1995b, *MNRAS*, 272, 885
Flin, P. 1986. in the *Proc of "The third Cracow Summer School of Cosmology"*, *Acta Cosmologica*, 14, 7
Hamilton, A.J.S. 1998, in *Ringberg Workshop on Large-Scale Structure*, ed. D. Hamilton (Kluwer, Amsterdam), 185
Hermit, S., Santiago, B.X., Lahav, O., Strauss, M.A., Davis, M., Dressler, A., & Huchra, J.P., 1996, *MNRAS*, 283, 709
Hoffman, G.L. & Salpeter, E.E., 1982, *ApJ*, 263, 485
Jenkins, A. *et al.* 1998, *ApJ*, 499, 20
Juszkiewicz, R., Vittorio, N., & Wyse, R. F. G. 1990, *ApJ*, 349, 408
Lahav, O., Fisher, K.B., Hoffman, Y., Scharf, C.A. & Zaroubi, S. 1994, *ApJ*, 423, L93
Lauberts, A. 1982, *The ESO/Uppsala Survey of the ESO(B) Atlas* (München: European Southern Observatory)
Lilje, P., Yahil A., & Jones, B., 1986, *ApJ*, 307, 91L
Lin, C. C., Mestel, L. & Shu, F.H. 1965, *ApJ*, 142, 1431
Loan A.J. 1997, PhD thesis, Cambridge University
Luo, S. & Vishniac, E. 1995, *ApJS*, 96, 429
Lynden-Bell, D. & Lahav, O. 1988, in *Large-Scale Motions in the Universe: A Vatican Study Week*, ed. V.C. Rubin & G.V. Coyne, Princeton University Press, Princeton 199.
Lynden-Bell, D., Faber, S.M., Burstein, D., Davies, R.L., Dressler, A., Terlevich, R.J., & Wegner, G. 1988, *ApJ*, 326, 19
Mecke, K.R., Buchert, T., & Wagner, H. 1994, *A&A*, 288, 697
Murtagh, F. & Heck, A., 1987, *Multivariate Data Analysis*, (Dordrecht: Reidel)
Nilson, P. 1973, *The Uppsala General Catalogue of Galaxies*, *Ann. Uppsala Astron. Obs. Band 6, Ser. V:A. Vol 1.*
Raychaudhury, S. 1989, PhD thesis, Cambridge University.
Rubin, V. 1951, *AJ*, 56, 47
Rubin, V. 1989, in *The World of Galaxies*, (New York: Springer-Verlag), 431
Sahni, V., Sathyaprakash, B.S. & Shandarin, S.F., 1998, *ApJ*, 495, L5
Santiago, B.X., Strauss, M.A., Lahav, O., Davis, M., Dressler, A., & Huchra, J.P. 1995, *ApJ*, 446, 457
Santiago, B.X., Strauss, M.A., Lahav, O., Davis, M., Dressler, A., & Huchra, J.P. 1996, *ApJ*, 461, 38
Sathyaprakash, B.S., Sahni, V., Shandarin, S.F. & Fisher, K.B., *ApJ Let*, in press (astro-ph/9805265)
Saunders *et al.* 1991, *Nature*, 342, 32
Scaramella, R. *et al.*, 1992, *ApJ*, 390, L57
Shaver P.A., & Pierre M. 1989, *A&A*, 220, 35
Stanev, T., Biermann, P.L., Lloyd-Evans, J., Rachen, J.P., & Watson, A. 1995, *PRL*, 75, 3056
Strauss M.A., & Willick J.A. 1995, *Phys. Rep.*, 261, 271
Strauss M.A., Yahil A., Davis M., Huchra J.P., & Fisher K.B. 1992, *ApJ*, 397, 395
Tully, B.R. 1986, *ApJ*, 303, 25
Tully, B.R. 1987, *ApJ*, 323, 1
Tully, B.R. & Shaya, E., 1984, *ApJ*, 281, 56
Waxman, E., Fisher, K.B., & Piran, T. 1997, *ApJ*, 483, 1
Webster, A.M. 1998, PhD thesis, Cambridge University.
Webster A.M., Lahav O., & Fisher K.B. 1997, *MNRAS*, 287, 425
White, S.D.M. & Silk, J. 1979, *ApJ*, 231, 1
Yahil, A., Strauss, M.A., Davis, M., & Huchra, J.P. 1991, *ApJ*, 372, 380
Zeldovich, Y.B. 1970, *A&A*, 5, 84